3D wave-resolving simulation of sandbar migration

Patrick Marchesiello, Julien Chauchat, Hassan Shafiei, Rafael Almar, Rachid Benshila, Franck Dumas

▶ **To cite this version:**

Patrick Marchesiello, Julien Chauchat, Hassan Shafiei, Rafael Almar, Rachid Benshila, et al.. 3D wave-resolving simulation of sandbar migration. 2021. hal-03345439v1

HAL Id: hal-03345439
https://hal.science/hal-03345439v1

Preprint submitted on 15 Sep 2021 (v1), last revised 10 Oct 2022 (v2)

HAL is a multi-disciplinary open access archive for the deposit and dissemination of scientific research documents, whether they are published or not. The documents may come from teaching and research institutions in France or abroad, or from public or private research centers.

L'archive ouverte pluridisciplinaire **HAL**, est destinée au dépôt et à la diffusion de documents scientifiques de niveau recherche, publiés ou non, émanant des établissements d'enseignement et de recherche français ou étrangers, des laboratoires publics ou privés.

3D wave-resolving simulation of sandbar migration

Patrick Marchesiello[a,*], Julien Chauchat[b], Hassan Shafiei[b], Rafael Almar[a], Rachid Benshila[c], Franck Dumas[d]

[a] *IRD/LEGOS, Toulouse, France*
[b] *Univ. Grenoble Alpes, CNRS, Grenoble INP, LEGI, 38000 Grenoble, France*
[c] *CNRS/LEGOS, Toulouse, France*
[d] *SHOM, Brest, France*

Abstract

The problem of sandbar migration on the storm timescale is revisited with a 3D wave-resolving hydro-sedimentary model. The model accurately simulates the successive offshore and onshore bar migration observed in a large-scale flume experiment (LIP11D) in response to wave forcing representing storm and post-storm (recovery) conditions. The diagnosis of sand transport and the analysis of a composite asymmetric wave cycle reveal the migration mechanisms in each phase. In all cases, sediment resuspension is dominated by breaking-induced turbulence, while net sediment transport and bed profile evolution are primarily the result of undertow distribution across the sandbar, rather than a trade-off between onshore and offshore fluxes. In the erosion phase, a strong undertow carries the mobilized sediment seaward of the bar crest. In the accretion phase, the sandbar becomes the breaking point to more moderate waves and the undertow is limited to the lee-side of the bar, causing an counterflow migration of the bar crest. The contribution of wave-related onshore fluxes is significant in this case – although secondary in magnitude – and coincide with higher mobilization and currents during the wave crest period. We conclude that computationally efficient 3D wave-resolving models (including morphological acceleration) can be used to improve our understanding of nearshore morphodynamic problems in realistic applications.

Keywords: nearshore, sandbar migration, wave-resolving model, wave asymmetry, sediment transport

1. Introduction

The presence of nearshore sandbars are ubiquitous on natural beaches, which are prime areas for morphological changes, depending on wave and sediment characteristics (Roelvink and Stive, 1989; Thornton et al., 1996; Elgar et al., 2001; Almar et al., 2010; Grasso et al., 2011). However, they present a challenge to our understanding of sediment transport processes, which is often based on the study of non-breaking waves (Scott et al., 2009; van der Zanden et al., 2017; Lim et al., 2020). The advantage of numerical models is their ease of application, but they usually rely on many assumptions and unknown parameters, so many aspects of bar dynamics remain unclear (Roelvink et al., 2012). In particular, the role of wave asymmetry on bar migration is debated (Grasso et al., 2011). Velocity skewness (sharp, high crests and broad, shallow troughs) and asymmetry (saw tooth-type waves) are considered to be responsible for sediment transport in the direction of wave propagation (onshore). The basic idea is that fast crest velocities in the onshore direction would mobilize and transport more sediment than the offshore-directed trough velocities (Hsu and Hanes, 2004). Wave asymmetry with its steep front would more efficiently mobilize sediments than skewed waves (Drake and Calantoni, 2001), possibly also reducing the phase lag between mobilization and transport (Dohmen-Janssen et al., 2002). Breaking waves may also contribute to bed shear stress asymmetry due to possibly higher turbulence intensity during the wave crest period (Ting and Kirby, 1994), although this process is disputed (Scott et al., 2009). Interestingly, it is generally assumed that bar migration results from a trade-off between onshore and offshore fluxes (e.g., Grasso et al. 2011), thus confusing the notions of convergent and confluent fluxes. A comprehensive conceptual model that could describe the interaction between onshore and offshore transport processes in bar migration, allowing for variable wave forcing, is still needed. The present work is a step in that direction. It will confirm the existence of wave-related onshore transport (especially in the accretion phase) but will show that sediment transport around the sandbar depends primarily on the cross-shore distribution of the undertow, which varies with wave height.

*Corresponding author
Email address: patrick.marchesiello@ird.fr (Patrick Marchesiello)

Two-phase flow models (water and sediment) applied to individual wave breaking can be used to describe hydro-morphodynamics in much details (Cheng et al., 2017; Kim et al., 2019), but are computationally very expensive. Therefore, the study of sandbar formation and migration was made in the past with much simpler, wave-averaged models (Watanabe, 1982; Stive, 1986; Roelvink and Stive, 1989; van Rijn et al., 2003), which are still in use — XBeach being a classic example (Rafati et al., 2021). These models rely heavily on parametrizations to account for both onshore and offshore sandbar migration, i.e., a balance between offshore transport by the undertow and onshore transport by skewed/asymmetric waves and wave streaming. Depth-dependent nearshore models (McWilliams et al., 2004) have improved the representation of the undertow, but the effects of wave asymmetry/skewness remain parametrized as bedload transport in the wave boundary layer (e.g., van der Werf et al. 2015 for Delft3D; Kalra et al. 2019 for ROMS). Recently, empirical formulations have improved, using the concept of half-wave cycles (Dibajnia and Watanabe, 1992; van der A et al., 2013), and are implemented with mixed success (Veen, 2014; Schnitzler, 2015). As an intermediate approach between expensive wave-resolving two-phase flow models and highly parametrized wave-averaged models, we propose to apply a wave-resolving, free-surface, coupled hydro-sedimentary model. CROCO (Coastal and Regional Ocean Community model) has recently been adapted to nearshore wave dynamics and circulation problems (Marchesiello et al., 2021). This cost-effective 3D wave-resolving model can explicitly simulated the vertical profiles of oscillatory cross-shore sediment transport, allowing assessment of the combined effects of mean undertow and asymmetric waves around a sandbar.

This paper presents a brief overview of the CROCO coupled hydro-sedimentary model, before discussing its application to a large-scale flume experiment (LIP11D), and an analysis of offshore and onshore sandbar migration under wave forcing representing storm and post-storm (recovery) conditions.

2. Model description

Due to limited computational resources, 3D wave-resolving models are still rarely used to study nearshore dynamics in realistic environments. Early applications starting in the 1990s

used the volume-of-fluid (VOF) method for free-surface tracking (e.g., Lin and Liu 1998; Watanabe and Saeki 1999; Derakhti and Kirby 2014; Larsen et al. 2020). This model type with Cartesian coordinate, where the free surface crosses computational cells arbitrarily, fails to precisely apply the pressure boundary condition on the free surface, affecting the model accuracy.

More recently, several 3D wave-resolving, free-surface and terrain-following RANS models have emerged for the nearshore zone, e.g., SWASH (Zijlema et al., 2011), NHWAVE (Derakhti et al., 2016), and CROCO (Marchesiello et al., 2021). In this case, the explicit overturning of the free surface is excluded and the breaking wave is modeled with a single-valued free surface which follows a shock process and resembles a dissipating bore. Despite the absence of explicit overturning (replaced by parametrized turbulence), these models can be accurate as well as computationally efficient (orders of magnitude cheaper) in the study of waves and wave-driven mean and transient circulation.

CROCO (`www.croco-ocean.org`) belongs to this class of models but, contrary to the other attempts, it solves the compressible Navier-Stokes equations (Auclair et al., 2018). A compressible approach preserves the hyperbolic nature of Navier-Stokes equations and does not require a global elliptic solver with incremental pressure corrections to ensure the incompressible mass balance. As a result, it avoids splitting errors between pressure and velocity and approximations made on free-surface conditions (Zijlema et al., 2011; Derakhti et al., 2016), thereby preserving amplitude and nonlinear dispersive properties of surface waves. In the same time, the absence of global computations by an elliptic solver makes optimization and parallelization procedures much more efficient (excellent scalability even on massively parallel computers). The cost of solving acoustic waves is managed with a time-splitting technique and semi-implicit time discretization.

2.1. Model equations

The full set of Navier-Stokes equations for a free-surface ocean is explicitly integrated in the nonhydrostatic, non-Boussinesq (compressible) version of CROCO, built on the code structure of ROMS primitive equation solver (Shchepetkin and McWilliams, 2005; Debreu

et al., 2012). Non-Boussinesq equations include the momentum and continuity equations, the surface kinematic relation (for free surface), heat, salt or other tracer C (such as sediment concentration) conservation equations, and the equation of state, which reads in Cartesian coordinates:

$$\frac{\partial \rho u}{\partial t} = -\vec{\nabla}.(\rho \vec{\mathbf{v}} u) + \rho f v - \rho \tilde{f} w - \frac{\partial P}{\partial x} + \mathcal{F}_u + \mathcal{D}_u + \lambda \frac{\partial \vec{\nabla}.\vec{\mathbf{v}}}{\partial x} \tag{1}$$

$$\frac{\partial \rho v}{\partial t} = -\vec{\nabla}.(\rho \vec{\mathbf{v}} v) - \rho f u - \frac{\partial P}{\partial y} + \mathcal{F}_v + \mathcal{D}_v + \lambda \frac{\partial \vec{\nabla}.\vec{\mathbf{v}}}{\partial y} \tag{2}$$

$$\frac{\partial \rho w}{\partial t} = -\vec{\nabla}.(\rho \vec{\mathbf{v}} w) + \rho \tilde{f} u - \frac{\partial P}{\partial z} - \rho g + \mathcal{F}_w + \mathcal{D}_w + \lambda \frac{\partial (\vec{\nabla}.\vec{\mathbf{v}})}{\partial z} \tag{3}$$

$$\frac{\partial \rho}{\partial t} = -\vec{\nabla}.(\rho \vec{\mathbf{v}}) \tag{4}$$

$$\frac{\partial \eta}{\partial t} = \ w|_{z=\eta} - \vec{\mathbf{v}}|_{z=\eta}.\vec{\nabla}\eta \tag{5}$$

$$\frac{\partial \rho C}{\partial t} = -\vec{\nabla}.(\rho \vec{\mathbf{v}} C) + \mathcal{F}_C + \mathcal{D}_C \tag{6}$$

(u, v, w) are the (x,y,z) components of vector velocity $\vec{\mathbf{v}}$; η is the free surface; P the total pressure; ρ the density; $f(x, y)$ and $\tilde{f}(x, y)$ are the traditional and non-traditional Coriolis parameters, function of latitude; g is acceleration of gravity; $\mathcal{D}_u, \mathcal{D}_v, \mathcal{D}_C$ are eddy-diffusion terms requiring second-moment turbulence closure models; $\mathcal{F}_u, \mathcal{F}_v, \mathcal{F}_C$ are forcing terms; λ is the second (bulk) viscosity, associated with compressibility (used to damp acoustic waves).

In this study, movements are produced along a channel by a wave generator in a homogeneous non-rotating fluid. In this case, the longitudinal flow equation v disappears and the Coriolis force, the baroclinic pressure force, and all surface fluxes are zero. There is no temperature or salinity stratification so that the associated density is constant in time and space (but not the dynamic density associated with acoustic waves).

2.2. Computational procedure

In the above set of equations, a relation between ρ and P is required. To that end, and as part of a time-splitting approach, density is decomposed into slow and fast components based on a first-order linear decomposition with respect to total pressure. The Navier-Stokes equations are then integrated with two different time steps within the time-splitting approach inherited from ROMS. The slow-mode integration is similar to ROMS, with the addition of the slow part of vertical momentum equation, while fast-mode integration is in 3D and includes the compressible terms of momentum and continuity equations. More details can be found in Auclair et al. (2018) and Marchesiello et al. (2021).

Note that acoustic waves can become pseudo-acoustic if their phase speed $c_s = \frac{\partial P}{\partial \rho}$ is artificially reduced (to be safe, no less than about 5 times the shallow-water phase speed). In this case, high-frequency processes associated with bulk compressibility may be non-physical, but an accurate solution for slower nonhydrostatic dynamics can be preserved, while relaxing CFL constraints. In our nearshore applications, a c_s value of 100 m/s instead of 1500 m/s makes almost no difference for the physical solution but allows a great reduction in the computational time (by half).

CROCO is discretized on a C-grid with finite-difference methods for slow and fast modes (Shchepetkin and McWilliams, 2005; Soufflet et al., 2016). In short, the slow-mode time-stepping algorithm is a Leapfrog Adams-Moulton predictor-corrector scheme, that is third-order accurate for integrating advective terms. The fast mode is integrated with a generalized forward-backward scheme, which is also third-order accurate. Vertical flux terms that do not require accuracy (vertical diffusion term in the slow mode and all acoustic terms of the w equation in the fast mode) are computed with an implicit time stepping to increase computational stability.

Horizontal and vertical advection terms are discretized using the WENO5-Z improved version of the 5th-order weighted essentially non-oscillatory scheme (Borges et al., 2008), which is popular for hyperbolic problems containing both shocks and smooth structures. WENO5-Z naturally copes with dispersive numerical modes as well as shocks caused by breaking waves, with no need for *ad hoc* criteria.

2.3. Turbulence closure

Along with the numerical treatment of breaking waves, a k-ϵ or k-ω model, solving the closure equations for turbulent kinetic energy k and dissipation ϵ or dissipation rate $\omega \propto \epsilon\, k^{-1}$, is used as part of a Generic Length Scale (GLS) method (Warner et al., 2005). In the absence of buoyancy forcing, the turbulence equations express a balance between transport, diffusion, shear production and dissipation:

$$\frac{\partial \rho k}{\partial t} = -\vec{\nabla}.(\rho \vec{\mathbf{v}}\, k) + \mathcal{D}_k + \rho(P - \epsilon) \tag{7}$$

$$\frac{\partial \rho \epsilon}{\partial t} = -\vec{\nabla}.(\rho \vec{\mathbf{v}}\, \epsilon) + \mathcal{D}_\epsilon + \rho \frac{\epsilon}{k}(c_{\epsilon 1} P - c_{\epsilon 2}\epsilon) \tag{8}$$

or

$$\frac{\partial \rho \omega}{\partial t} = -\vec{\nabla}.(\rho \vec{\mathbf{v}}\, \omega) + \mathcal{D}_\omega + \rho \frac{\omega}{k}(c_{\omega 1} P - c_{\omega 2}\epsilon) \tag{9}$$

The eddy viscosity $\nu_t = c_\mu\, l\, k^{\frac{1}{2}}$ is derived from these equations, with coefficient c_μ dependent on stability functions, and mixing length $l \propto k^{\frac{3}{2}} \epsilon^{-1}$. l is resolution independent, which is consistent with a RANS rather than LES approach. The shear production term for k is $P = 2\nu_t S_{ij} S_{ij}$, with the mean strain rate tensor $S_{ij} = \frac{1}{2}(\frac{\partial u_i}{\partial x_j} + \frac{\partial u_j}{\partial x_i})$ (using Einstein notation). All turbulence model parameters are given in Warner et al. (2005), based on Burchard et al. (1998) for k-ϵ and Wilcox (1988) for k-ω. The only present modification concerns the surface and bottom mixing lengths, which are model boundary conditions given by: $l_s = \kappa z_{0s}$ and $l_b = \kappa z_{0b}$. We found that a relatively high value of z_{0b} (5 cm) is needed to match the observed sand concentration profiles near the bottom. With the k-ϵ model, the momentum mixing is also sensitive to z_{0s}, which needs to be increased to 0.2 m in order to match the observed velocity profiles (see validation section 3.3). For this reason, and for its robustness through resolutions, the k-ω model will be our standard turbulence model.

2.4. Wave maker at offshore boundary

The wave maker forces a spectrum of linear waves at the offshore boundary, as in Zijlema et al. (2011). In full 3D applications, the spectrum has frequency and directional spreading

Marchesiello et al. (2021) but in this flume experiment, waves are shore normal:

$$\eta_{bc}(t) = \sum_i a_i \, \cos(\omega_i \, t + \phi_i) \tag{10}$$

$$u_{bc}(z,t) = \eta_{bc}(y,t) \; \omega_p \; \frac{\cosh(k_p(z+h))}{\sinh(k_p h)} \tag{11}$$

where (x,y,z) are cross-shore, alongshore and vertical directions respectively; (i) is the index of spectral distribution; a_i is the amplitude at each frequency ω_i, from a given statistical distribution, e.g., JONSWAP (Sec. 3.2); ω_p and k_p are peak frequency and wavenumber related by the linear dispersion relation: $\omega_p^2 = g \, k_p \, \tanh(k_p h)$ with h the water depth; ϕ_i is a uniformly distributed random phase.

w_{bc} is set to zero and our tests show only weak sensitivity to this choice. Depth-averaged (barotropic) velocities $(\bar{u}, \bar{v})$ must be provided as well in the wave maker because they are prognostic variables, advanced together with the fast acoustic mode. Normal depth-averaged velocity $\bar{u}$ is complemented at the boundary by an anti-Stokes "compensation flow", opposite to Stokes drift and thus closing the volume budget. We do not impose the depth-averaged value of u_{bc} directly but through the incoming characteristic of the shallow water system as in Flather-type conditions (Marchesiello et al., 2001; Blayo and Debreu, 2005):

$$\bar{u} = \bar{u}_{bc} - \sqrt{\frac{g}{h}}(\eta - \eta_{bc}) \tag{12}$$

This allows infragravity waves generated inside the domain to propagate out as long waves, while ensuring a near conservation of mass and energy through the open boundary. Likewise, the baroclinic components (u_{bc}, w_{bc}) are applied via an adaptive radiation condition which helps short waves and 3D flow perturbations to leave the domain with only a small effect on the interior solution (Marchesiello et al., 2001).

2.5. Sediment and bed model

CROCO comes with capabilities for water quality, marine ecosystem and sediment modeling. They are built upon Eq. 6 for the transport of tracer concentration but, in the case of sediment modeling, additional sources and sinks are needed to simulate the exchange

between the water column and sediment bed (Blaas et al., 2007; Warner et al., 2008). Neglecting compressibility ($\rho \sim \rho_0$), the sediment concentration follows:

$$\underbrace{\frac{\partial C}{\partial t}}_{RATE} = - \underbrace{\vec{\nabla}.\vec{\mathbf{v}}C}_{ADVECTION} + \underbrace{\mathcal{D}_C}_{MIXING} - \underbrace{\frac{\partial w_s C}{\partial z}}_{SETTLING} + \underbrace{\frac{E}{\delta z_b}\Big|_{z=z_b}}_{EROSION} \tag{13}$$

w_s is the settling velocity, dependent on sediment grain size, but not on flow conditions and concentrations (Soulsby, 1997). Settling is computed via a semi-Lagrangian advective flux algorithm, which is unconditionally stable (Durran, 2010). It uses a piece-wise parabolic vertical reconstruction of the suspended sediment for high-order interpolation, with WENO constraints to avoid oscillations. E is the erosion flux at the sea floor and is only applied to the first grid level of height z_b and cell size δz_b.

In the present study, this suspended sediment model is used with simple settings. It is composed of a single fine sand class with settling velocity w_s=2.5 cm s^{-1} (grain size d_{50}=0.22 mm). For resuspension, taking one sediment bed layer for simplicity, only two parameters are needed: critical shear stress τ_{cr} and erosion rate E_0 at the seafloor, expressed in the erosion flux (Blaas et al., 2007):

$$E = E_0(1-p)\,\frac{\tau_b - \tau_{cr}}{\tau_{cr}} \quad \text{for } \tau_b > \tau_{cr} \tag{14}$$

E_0 is set empirically to 5.10^{-3} kg m^{-2} s^{-1} (Smith and McLean, 1977); p is the sediment porosity (0.41); τ_{cr}, the critical shear stress, i.e., the threshold for initiation of sediment motion, is set to 0.11 N m^{-2} (Soulsby and Whitehouse, 1997). τ_b is the bottom shear stress estimated from the logarithmic law of the wall:

$$\vec{\tau_b} = \frac{\kappa^2}{\log^2(\frac{z_b}{z_{0b}})}\,|u_b|\,\vec{u_b} \tag{15}$$

$|u_b|$ and $\vec{u_b}$ are the magnitude and vector of oceanic bottom currents in the log layer at a height z_b above bed; $\kappa = 0.41$ is the Von Karman constant; and z_{0b} is the bottom roughness length.

In the surfzone, the effect of wave-breaking, especially plunging breakers over sandbars, on sediment resuspension needs to be addressed (Voulgaris and Collins, 2000; van der Zanden

et al., 2017; Otsuka et al., 2017; Lim et al., 2020). Lim et al. (2020) suggest a strong correlation between the maximum sediment concentration observed in the LIP experiment and the plunging point (about 10 m downstream of the breaking point) over the sandbar. We adopt here the approach proposed by Reniers et al. (2004) consisting in replacing $|u_b|$ by an stirring velocity reinforced by the turbulence motion induced by wave breaking:

$$\begin{aligned} u_{stir} &= \sqrt{u_b^2 + u_t^2} \\ u_t &= \phi(x)\, \alpha_{br} \sqrt{k_b} \end{aligned} \tag{16}$$

The subgrid bottom turbulent kinetic energy k_b is given by the turbulence model and α_{br} is a factor explaining the effectiveness of breaking waves in the entrainment of bottom sediments. We used a common value of $\alpha_{br} = 10$ (Ribas et al., 2011), which produces sand concentrations close to observations in both the erosive and accretive phases. $\phi(x)$ is a Gaussian function centered around the plunging point in order to enhance the turbulence effect at this position. This part is the only non-generic aspect of the model presented here but is essential to reproduce the correct profiles of sediment concentrations — and in turn a requirement for accurate bar migration. We have tried alternative and more generic methods of resuspension by plunging breakers with some success (see Discussion section) but a more dedicated study is needed for what appears to be a real challenge.

Estimating z_{0b} is not trivial with moving sediment and various empirical formulations exist that account for roughness over a mobile bed (Wiberg and Rubin, 1989). They generally assume that grain roughness is the most important predictor for the onset of sand suspension, but bedload and ripple form roughness are also considered (Li and Amos, 2001). Here we use grain roughness.

For bedload transport, we do not rely on parametrization as skewed-asymmetric waves are resolved explicitly, but we make sure that the wave-boundary layer is resolved, and that the first vertical level is in a sheet flow layer (about 10 times the grain size). This is particularly important for the onshore bar migration phase. Note that in our formulation, the turbulence intensity (calculated with the closure model) only affects sediment resuspension, not deposition, as in, for example, Kawanisi and Shiozaki (2008)).

The bed model accounts for changes in sea floor elevation resulting from convergence or divergence in sediment fluxes (Exner equation):

$$\frac{\partial h}{\partial t} = -\frac{f_m}{\rho_s(1-p)}\left(w_s C - E\right) \tag{17}$$

ρ_s is sediment density and f_m is a morphological acceleration factor (Roelvink, 2006) described below. Morphological changes can have a significant influence on flow and transport when they are greater than a few percent of the water depth. Morphological updating strategies are described by Roelvink (2006) and implemented in CROCO following Warner et al. (2008). For dynamical consistency, the vertical velocity is modified by the rate of change of vertical grid levels dz/dt, adjusting to the moving sea floor and free surface (grid "breathing" component; Shchepetkin and McWilliams 2005). This method is mass conserving and retains tracer constancy preservation.

Morphological acceleration can be achieved with no constraint on the model time step by multiplying erosion and deposition rates by the scale factor f_m at the bed-water interface (Eq. 17). Only the fluxes to and from the bed are changed, not the magnitude of the sediment concentrations in the water column. To our knowledge, this paper presents the first use of a morphological acceleration technique with a wave-resolving model. We have found that the technique is effective since we obtain the same result with or without morphological acceleration. We were able to use a large morphological factor f_m (at least up to 64) because the timescale of morphodynamics (here bar migration) is slow compared to that of wave dynamics.

3. Simulation of a large-scale flume experiment

We now present our model solution of sandbar migration, applied to the European Large Installation Plan (LIP) experiments, which was carried out at full scale in Delft Hydraulics's Delta Flume (Roelvink and Reniers, 1995). We first present the model setup for these experiments, the model validation of current profiles, then the comparative analysis of offshore and onshore bar migration.

In Marchesiello et al. (2021), the model's ability to simulate surface gravity wave propagation, nearshore breaking and the resulting circulation was validated against laboratory experiments. In particular, the GLOBEX experiment (Michallet et al., 2014) provided high-resolution measurements of surface wave height η and bottom currents u_b. A comparison was made of continuous profiles of wave statistics for η and u_b across the beach. The model statistics closely resembled the measurement data (in structure and magnitude), including high-order moments, showing the transition from skewness to asymmetry across the surf-zone. We will not repeat this comparative study here but wish to build on it to emphasize the model's good representation of wave asymmetry, which is important for the onshore bar migration.

3.1. LIP experiment

The Flume is 225 m long, 5 m wide and 7 m deep. In LIP, three types of experiments were carried out under different types of irregular waves, which subsequently resulted in a stable (1A), erosive (1B), and accretive (1C) beach state (see Table 1 and Roelvink and Reniers 1995 for details). The initial profile is linear in LIP-1A, with a slope of 1:30 and consisting of a median grain size of 0.22 mm. The final profile of LIP-1A was used as the initial profile of LIP-1B and the final profile of LIP-1B as the initial profile of LIP-1C. The wave conditions were a JONSWAP narrow-banded random wave spectrum generated by a wave paddle, with a peak enhancement factor $\gamma = 3.3$ and characteristic wave height and period: $H_s = 1.4$ m, $T_p = 5$ s (LIP-1B) and $H_s = 0.6$ m, $T_p = 8$ s (LIP-1C). Under this wave forcing, the sandbar developed during LIP-1B, increasing in height and migrating in the offshore direction. Under the accretive conditions of LIP-1C, the bar migration reversed to the onshore direction. The bed profile was measured with a profile follower that used an automated sounding system. Wave-averaged current profiles were captured by a movable carriage with attached current meters starting 10 cm above the bed and at 10 locations along the flume (2 cm/s accuracy). Similar profiles of wave-averaged concentrations of suspended sediment were measured by suction tubes mounted on a carriage starting 5 cm above the bed (10% accuracy). For validation of currents and sand concentration, we consider the

time 8 hours after initialization in experiment 1B and 7 hours in 1C (Veen, 2014).

3.2. Model setup

The model setup is adapted from the LIP experiment. A JONSWAP wave spectrum similar to the experiment is generated with shore normal direction and zero directional spread. A no-slip condition is imposed on the lateral wall boundaries of the canal so that transverse modes are precluded. The grid spacing is dx=25 cm with 10 vertical levels with refinement at the bottom. This vertical refinement is important for wave-related transport, while the results were poorly sensitive to horizontal resolution (a test with dx=50 cm and 1 m is presented below). The model time step is dt = 25 ms. The minimum depth is 1 mm on the shore, the position of which varies with the swash oscillation, relying on a wetting-drying scheme (Warner et al., 2013). For bed skin shear stress (setting sediment in motion), the logarithmic law of the wall is used with grain roughness $z_{0s} \sim D50/12 = 0.02$ mm. To account for increased momentum friction due to near-bed sediment suspension (e.g., Suarez et al. 2014), we increase the roughness length for momentum to 0.2 mm.

The LIP-1B and LIP-1C experiments lasted 18 and 13 hours, respectively. In both cases, the model was run for one hour with a morphological acceleration factor f_m equal to 18 and 13 respectively. Since the results were similar without acceleration, the acceleration technique allowed us to perform many sensitivity tests.

3.3. Turbulence model validation

An important process for offshore bar migration is the suspended load transport by the undertow. To assess the model hydrodynamics in the LIP configuration, we present a comparison of current profiles taken after 8 hours in experiment 1B and averaged over one hour. It will also be a test for our numerical wave maker in its ability to generate a spectrum of random waves.

Figure 1 shows a comparison of the model with data, using our standard configuration. The match with measured currents is very good throughout the complex morphology of the beach. The waves start to break before reaching the sandbar, but the breaking is more

intense on the sandbar. The resulting velocity profile on the lee-side of the bar has a high shear and the undertow has an intensity above 30 cm/s. The horizontal resolution test (25 cm, 50 cm and 1 m) shows a mean error of about 3 cm/s at all resolutions, close to the measurement error of 2 cm/s. The results are thus consistent at all resolutions despite no adjustment of any parameter. It confirms the validity of a RANS approach for estimating the mixing length of breaking-induced turbulence.

Turbulent kinetic energy and eddy viscosity estimated by the k-ω model in the breaker zone have the expected structure (Fig. 1; top) and magnitude ($\nu_t \sim 0.01h\sqrt{gh}$; Svendsen 1987; Cox et al. 1994). Interestingly, the transport terms in the closure equations tend to reduce mixing at the break point by redistributing the turbulent energy, thus allowing more intense shear to be maintained (not shown). The k-ϵ model works almost as well as the k-ω model, with respect to mean current profiles, but the comparison is improved by imposing a high value on the surface mixing length (z_{0s}=0.2 m), as in wave-averaged models (Feddersen and Trowbridge, 2005). The k-ω model may thus be a better choice for surface wave breaking, possibly due to a more accurate near wall treatment (Mayer and Madsen, 2000; Devolder et al., 2018; Larsen et al., 2020). Note, however, that this model produces a greater amount of mixing in potential flow regions outside the surf zone (innershelf), mainly due to the divergence part of the mean strain rate tensor (Mayer and Madsen, 2000).

3.4. Currents and suspended sediments

To analyse the model for different conditions, two experiments are selected, namely LIP-1B and the LIP-1C cases (Table 1). Figure 2 shows a model-data comparison of wave height H_{rms} for the two experiments. The data is reproduced accurately. High waves in LIP-1B ($H_s = 1.4$ m, $T_p = 5$ s) caused beach erosion while, in LIP-1C, moderate waves ($H_s = 0.6$ m, $T_p = 8$ s) caused an accretive beach.

We are first interested in the erosion phase where the sandbar moves offshore under the effect of high waves. The LIP dataset is used for comparison purposes, containing velocity and concentration profiles as well as bed level evolution (see next section). Figure 3 shows a comparison of wave-mean velocity and concentration profiles for LIP-1B. As for

velocity profiles presented in the validation section, sediment concentrations also show a very good match between model and data. The high concentrations over the sandbar crest and trough are triggered by a large bed shear stress associated with a combination of wave-mean undertow, wave oscillatory flow and turbulent velocity.

Note that waves and associated orbital velocities are greatest off the sandbar. However, the maximum suspended sand concentration is not found offshore but coincides instead with a maximum in turbulence intensity and undertow speed inshore of the bar crest. This is in contrast to parametrizations more suited to shelf dynamics, where sediment erosion responds to the addition of bed shear stresses by currents and waves. (e.g., Soulsby 1995).

The model simulation of the accretive phase is also reproduced accurately (Figure 4). In this case, wave breaking occurs right on the sand bar. The currents are thus weaker off the bar, but the undertow inside the bar remains quite strong. The suspended sand concentration is also significant there, although weaker than in the erosive phase.

3.5. Offshore and onshore sandbar migration

Figure 5 (top) shows the bed evolution 18 hours after the start of experiment 1B, with the corresponding section of wave-mean cross-shore currents. Some small discrepancies are visible but the offshore sandbar migration is correctly reproduced in terms of distance of migration and height of the bar. The maximum undertow magnitude (-0.3 m/s) follows the lee-side slope of the bar and appears as the driver of its migration. A secondary undertow maximum is visible on the terrace of the inner surfzone and appears to coincide with an offshore spreading of the terrace. In the outer surfzone (off of the main sandbar), a second smaller bar forms both in the model and in the measurements during LIP-1B (at a position of about 70 m), corresponding to a weakened undertow.

The bottom panel of Figure 5 shows the result of the accretive phase LIP-1C when waves have lower amplitude, with an opposite migration directed towards the shore. In this case, the flow structure is very similar but weaker and the bar seems to migrate against the undertow. The latter is still able to bring sediment to the leeward slope of the bar, but the offshore slope and crest are moving inshore, creating an asymmetry in the bar shape.

Sediment transport processes are analyzed in more detail in the next section.

4. Sediment transport mechanisms

4.1. Sediment budget

The wave-mean sediment transport term $-\frac{1}{\rho_0}\overrightarrow{\nabla.(\rho\vec{\mathbf{v}}C)}$ — ρ_0 is a mean density, so that the transport term is in units of $\mathrm{kg/m^3/s}$ — is presented in Figure 6 for the time halfway between the erosive (top) or accretive (bottom) phase (averaged over a period of about 10 min). This confirms for LIP-1B that during high waves and strong undertow, a large amount of sand is removed from the lee-side slope and trough area – after being first suspended and stirred upward – and then transported to the offshore slope, where it settles. Part of this process is attenuated by surface transport, which brings back some sediment to the bar trough region. For LIP-1C, however, sand is removed from both the trough of the bar and the offshore slope (including the crest), and it converges to the inner slope. This transport may qualify as bedload or sheet-flow transport as it occurs primarily within the wave boundary layer of about 10 cm.

For further analysis, Figure 7 presents the depth-integrated suspended sediment budget, again for the erosive (top) or accretive (bottom) phase. The different terms of Eq. 13 are computed online, averaged in time and integrated along the vertical axis. The budget comes down to three main tendency terms: erosion-settling residual, advection, and rate of change (vertical mixing cancels out when integrated). Suspended sediments are close to equilibrium since the rate of change is generally much smaller than the other two terms, which tend to be opposite. This analysis confirms the difference between LIP-1B and LIP-1C, with transport limited to the lee side of the bar in LIP-1C. In LIP-1B, there is a dominant erosion process in the bar trough and offshore transport and deposition beyond the bar crest. In LIP-1C, the process is similar but transport and deposition are confined to the inshore side of the bar crest, while a secondary zone of net erosion appears on the offshore side (this secondary erosion also appears in LIP-1B but much further offshore).

In the next section, we distinguish between wave and mean current transport in order

to identify and quantify the role of asymmetric waves for bar migration, particularly in the accretion phase of LIP-1C.

4.2. Wave-related and current-related fluxes

For each experiment (erosive or accretive), we construct a wave composite by superposing instantaneous data over many wave cycles (about 50). To that end, the duration of all wave cycles must be fitted to the peak period, so that data averaging can be made over the different phases of a generic cycle. This composite is made at three locations around the sand bar: offshore slope, crest and trough (corresponding to positions: x=131, 139 and 148 m in LIP-1B; and x=129, 136 and 144 m in LIP-1C).

Starting with the more complex accretive case, Figure 8 (left panels) shows the currents and sand concentrations at the first model level (1-2 cm above bed) for the composited LIP-1C wave cycle. Here, the mean values are subtracted to retain the oscillatory flow and associated perturbed concentrations ($u' = u - \overline{u}$ and $C' = C - \overline{C}$). In addition, the figure shows the undertow u_b and effective turbulent velocity u_t entering the bed shear stress formulation. The currents have a typical skewed/asymmetric structure across the wave cycle. They are largely skewed over the offshore slope and become less skewed but more asymmetric as the wave progresses toward the shore. The largest sand concentrations are over the bar crest where it peaks about half a second after the peak velocity. The lag is similar for skewed velocity over the offshore slope, although the peak there is much weaker. The main reason is that the effective turbulent velocity is more than twice as large over the crest and more significantly contributes to the bed skin stress. The sand concentration cycle is different in the trough region, where the undertow becomes comparable in magnitude to the orbital velocities. The total onshore-directed flow is reduced during the crest half-cycle while the offshore-directed flow is increased during the trough half-cycle. As a result, positive resuspension anomalies are present during both phases of negative and positive wave velocities.

The right panels of Figure 8 show the profiles of suspended sand flux. The averaged flux over the composited wave cycle is separated into wave and mean components (Reynolds

decomposition): $\overline{uC} = \overline{u'C'} + \overline{u}\,\overline{C}$. The undertow being weak over the offshore slope and crest (Fig. 5, bottom panel), the total flux there is dominated by the residual wave flux, which is onshore (at least in the wave boundary layer, but the flux is slightly negative above). The maximum flux over the crest appears to coincide with a combination of high sand concentration (1 g/L) and positive velocities (1 m/s) during the wave crest period (middle-right panel of Fig. 8). Over the offshore slope, the velocity is more skewed than asymmetric and the concentration is limited by a weaker bed stress (due to weaker turbulence). The phase lag between mobilization and transport of sediment (Dohmen-Janssen et al., 2002) does not vary between the two positions (as expected from fast settling that gives a weak phase lag parameter) and therefore cannot explain the differences in sand flux. In the bar trough, the wave-related flux remains positive but its magnitude is much reduced. The reason is the second peak of sand resuspension during the wave trough phase (negative half-cycle), due to a strong undertow. An even stronger undertow could eventually reverse the sign of this flux (Scott et al., 2009).

The result of opposite onshore and offshore sand fluxes is a convergence of sediment between the trough and crest regions, which promotes an onshore bar migration. However, the bar takes on an asymmetric shape because the undertow plays a dominant role in the displacement of the bar crest.

In our simulations, wave-breaking turbulence contributes little to the onshore flux asymmetry, unlike in Ting and Kirby (1994). This is because, although more turbulent energy is generated at the surface during the wave crest period, a significant portion reaches the bottom during the trough of the next wave (Figure 1) and the bottom turbulent velocity in Figure 8 exhibits only small variations during the wave cycle. This tends to argue against a strong asymmetric effect of breaking turbulence, although we are aware that the turbulence model may misrepresent the role of plunging waves (i.e. the timing and efficiency with which they mobilize sediment). However, observations suggest that wave-breaking turbulence is sufficiently intermittent to lose some of its correlation with wave phase (Ruessink et al., 2011). Improvements could be made in this area.

Looking now at the LIP-1B erosive experiment (Fig. 9), we see a different dynamic,

which generalizes the mechanism described earlier for the trough region. Since the undertow is present at all locations, the total flux is also negative at all locations. The wave-related flux tends to be weaker than in LIP-1C because the negative undertow decreases resuspension in the positive orbital velocity phase (wave crest) and increases it in the negative phase. However, over the crest, a significant wave-related flux remains. Note that waves over the sandbar in LIP-1B (and their asymmetry; see next section and Fig. 11) are actually weaker than in the accretive phase, despite larger offshore waves. The reason is that, in this case, the waves break off the bar, where they lose much of their energy. However, the undertow extends across the sandbar and overwhelms the wave effect everywhere. Note also the strong sediment flux convergence on the offshore side of the bar despite a consistently negative sand flux. In other words, there need not be a confluence of onshore and offshore fluxes for flux convergence to occur.

4.3. Wave asymmetry

Figure 10 presents the profiles of current skewness and asymmetry for the three sandbar locations. Normalized values (right panel) are computed as $\langle u'^3 \rangle / \langle u'^2 \rangle^{1.5}$ for skewness and $\langle \mathcal{H}(u')^3 \rangle / \langle u'^2 \rangle^{1.5}$ for asymmetry. We also present the dimensional values (left panels), computed without normalization by the cube of standard deviations. It confirms the relatively high skewness and low asymmetry on the outer slope, relative to the bar crest. The dimensional values reveal a much higher absolute asymmetry on the bar crest, compared to the surrounding areas. This result is hidden in the dimensionless calculation. Bottom skewness on the slope is larger than asymmetry on the crest, but with less effect on the sand flux, as seen earlier. This would confirm the efficiency of asymmetry versus skewness, but in our case this is coincidental: the difference in sand flux is related to the varying intensity of turbulence across the bar, rather than a varying phase lag between mobilization and transport — sometimes associated with the transformation from skewness to asymmetry (Dohmen-Janssen et al., 2002). Our interpretation of the respective role of asymmetry and skewness thus involves a spatial correlation between wave asymmetry and breaking turbulence. Finally, the trough region is characterized by low absolute skewness and asymmetry near the

bed and the sand flux there is always driven by the undertow.

The dimensional skewness and asymmetry also reveal large vertical variations from surface to bottom. Wave skewness/asymmetry is intensified at the surface because wave velocities are greater, but the intensification is much larger for broken waves inshore of the bar. In this case, the wave velocities are also much stronger at the surface (1.2 m/s, as for shoaling waves) than at the bottom. Another noticeable point about these profiles is a slight decrease of dimensional skewness and asymmetry in the wave boundary layer, and a decrease of dimensionless asymmetry in favor of skewness, consistent with observations (Suarez et al., 2014). However, here, this transformation is weak and does not seem to play a significant role.

4.4. Bed shear stress

It is interesting at this point to test the validity of formulations used for bed skin stress in wave-averaged models (e.g., Blaas et al. 2007). The friction is generally parametrized as the addition of wave-induced (τ_w) and current-induced (τ_{cw}) bottom stresses (Soulsby, 1995). In the nearshore region (as confirmed here), the current-related friction has a lesser role and we will focus on the friction induced by wave orbital velocities and breaking turbulence:

$$\tau_w = 0.5\, f_w\, (u_w + u_t)^2 \tag{18}$$

with the friction factor of (Soulsby, 1995), but modulated by a constant r_f:

$$f_w = 1.4\, r_f \left(\frac{u_w}{\sigma z_{0b}} \right)^{-0.52} \tag{19}$$

u_w is the maximum bottom orbital velocity, determined from wave-mean wave characteristics. u_w accounts for skewness as a correction to the linear theory (Isobe and Horikawa, 1982; Abreu et al., 2010; Malarkey and Davies, 2012; Nam et al., 2020): $u_w = r_s u_w^{lin}$, where r_s is a skewness factor ($r_s = 1$ for linear waves). r_s can be obtained using empirical formulas involving a logarithmic relation with the Ursell number $Ur = H_s\lambda^2/h^3$, a measure of wave nonlinearity (Nam et al., 2020). Here, we use a slightly modified formula compared to Nam

et al. (2020): $r_s = 0.051 \log Ur + 0.84$. The turbulence stirring velocity u_t is computed as for the wave-resolving simulation (Eq. 16) but with wave-averaged k_b.

Figure 12 shows our attempt of reconstructing the simulated bed shear stress with parametrizations. At offshore positions, where waves are nearly linear, a value of $r_f = 0.4$ is required to fit the simulated bed shear stress reconstructed from Soulsby (1995). Then, in the nearshore region from about $x = 40$ m, the parametrized bed shear stress is underestimated with linear waves and no turbulence ($r_s = 1$ and $u_t = 0$). Adding skewness correction, the bed shear stress is recovered more accurately around the sandbar, particularly on the seaward side. The most striking feature is that turbulence stirring contributes most of the simulated stress on the sandbar (in the roller zone, downstream of the sandbar, the turbulence effect seems underestimated). This analysis thus confirms that consideration of wave asymmetry may be important but that turbulent mixing by plunging breakers is essential to mobilize significant sediment loads on the sandbar, allowing its realistic migration.

5. Discussion and conclusion

Analysing the interplay between wave-mean undertow and wave skewness/asymmetry in field measurements or even in physical models is a difficult task. Numerical modeling offers a complementary approach as long as their precision is not too compromised by unknown parameters. In the present study, we present the first application of a 3D wave-resolving hydro-sedimentary model to the case of bar migration. The simulation is that of a large-scale flume experiment comprising two phases: erosion (offshore bar migration) during high-wave conditions and accretion (onshore bar migration) during post-storm, moderate wave forcing. The model can faithfully reproduce in both cases the wave statistics, the profiles of wave-mean currents and sand concentrations, as well as the morphological evolution of the sand bed.

The Analysis of the transport mechanisms shows the importance of the undertow distribution around the sandbar. Its convergence and divergence patterns appear to have more impact on submerged beach morphology than the confluence of wave- and current-related

fluxes. In the erosion phase, in particular, the waves begin to break well ahead of the sandbar and a strong undertow causes the mobilized sediments to move in a near morphological translation. In this case, the wave-related transport is weak because sand mobilization, dominated by the undertow, is distributed almost uniformly between the two phases of the wave cycle. Much of the sediment is carried in suspension as the intensity of turbulence within the water column is high. It is interesting to note that there is a moderate surface flux of sediment towards the shore, carried by the breaker-induced onshore flow.

Under moderate wave action, the sandbar becomes a breaking point and the undertow is confined to the inshore area of the bar crest with a maximum on the inner slope. Because the bed shear stress and associated mixing is weaker in this case, the sand concentration is almost confined to a sheet flow layer. In comparison to more energetic wave conditions, the sandbar migrates onshore at a slower rate and with an asymmetric shape. This is the result of a combination of two mechanisms: the deposition of sand carried by the undertow on the inshore side and, to a lesser extent, onshore fluxes due to asymmetric waves on the offshore side. Note that these mechanisms are not opposed here, as is often suggested (Roelvink and Stive, 1989; Grasso et al., 2011), but complementary.

The composite analysis of wave skewness/asymmetry reveals that the onshore sediment flux is strongest over the bar crest where asymmetry produces a steep front with strong currents during the onshore half-cycle. Associated with these currents, the sand is resuspended within only half a second with much contribution by breaking turbulence. Over the offshore slope, where skewness is greater than asymmetry, a similar process is at work but is weaker due to weaker resuspension, and not because of a greater phase lag between mobilization and transport.

These results thus confirm a moderate role of wave-related onshore flow in the evolution of sandbars, and only under post-storm wave conditions, when the sandbar becomes a breakpoint. The role of bottom streaming is unclear. By increasing bottom friction (roughness increased to 1 mm), it becomes a player, although not a dominant one in our simulations (it contributes a few cm/s and hardly counteracts the undertow of about 30 cm/s over the bar, even in the accretive case).

The largest uncertainty in the model comes from the estimation of bed roughness and bed shear stress due wave-breaking turbulence. Clearly, sand mobilization (and transport) is unrealistic without turbulence, as already noted by van der Zanden et al. (2017) and Lim et al. (2020) for the same LIP experiments. Lim et al. (2020) suggested that a large local increase of suspended sand concentration in the LIP experiment could only be attributed to breaking wave turbulence and more precisely to plunging breaker vortices invading the wave bottom boundary layer. We followed the idea of Reniers et al. 2004 of adding a breaking-induced turbulent bottom current (from the turbulence model) to the bed shear stress formulation. Using an enhancement factor and positioning function for this turbulent motion leads to realistic results. The positioning function, however, lacks a generic type mechanism and efforts should be made in this direction. Among the alternatives we tried, we found promising results using power laws to locally enhance the effect of subgrid-scale turbulent energy. We also obtained similar results by setting the bottom stress as a function of the undertow (the undertow seems to be a good proxy due to its correlation with breaker dissipation; Faria et al. 2000). Additional work will likely be required, including explicit consideration of plunging breakers.

With these caveats in mind, our results nonetheless demonstrate the reliability of computationally efficient 3D wave-resolving models such as CROCO – intermediate between two-phase DNS and wave-averaged approaches – for addressing nearshore hydro-morphodynamic problems. They point out the deficiencies of the depth-averaged approach, with its hypersensitivity to bottom friction and rough estimation of the undertow, when its cross-shore distribution seems so important. Our wave resolution model can also help improve parametrizations in 3D wave-averaged models, in particular wave-related transport through the concept of wave half-cycles.

An interesting new result also comes from the morphological acceleration method, which is used here for the first time with a wave-resolving model. We demonstrated its applicability and were even able to use a factor as large as 64, because the timescale of morphodynamics (here bar migration) is slow compared to that of wave dynamics. This method is particularly interesting in terms of computational cost because it allows us to consider long period

simulations despite the choice to explicitly solve for waves. Therefore, the possibility of using strong morphological acceleration in a wave-resolving approach makes it a suitable alternative to wave-averaged models for realistic 3D applications.

Acknowledgement

This research has received support from a consortium of French research agencies, as part of CROCO's development project (Insu GdR n°2014 named CROCO) and from the French Naval Hydrographic and Oceanographic Service (SHOM DGA-Protevs II and MEPELS projects). It was granted access to the HPC resources of CALMIP supercomputing center under allocation P19069. We thank Dano Roelvink for sharing the LIP data. Apart from these, all data were acquired by the authors and the CROCO source code is freely available at `www.croco-ocean.org`. Both laboratory and modeling data are available upon request.

References

Abreu, T., Silva, P.A., Sancho, F., Temperville, A., 2010. Analytical approximate wave form for asymmetric waves. Coastal Engineering 57, 656–667.

Almar, R., Castelle, B., Ruessink, B.G., Sénéchal, N., Bonneton, P., Marieu, V., 2010. Two- and three-dimensional double-sandbar system behaviour under intense wave forcing and a meso–macro tidal range. Continental Shelf Research 30, 781–792.

Auclair, F., Bordois, L., Dossmann, Y., Duhaut, T., Paci, A., Ulses, C., Nguyen, C., 2018. A non-hydrostatic non-boussinesq algorithm for free-surface ocean modelling. Ocean Modelling 132.

Blaas, M., Dong, C., Marchesiello, P., McWilliams, J.C., Stolzenbach, K.D., 2007. Sediment-transport modeling on southern californian shelves: A ROMS case study. Continental Shelf Research 27, 832 – 853.

Blayo, E., Debreu, L., 2005. Revisiting open boundary conditions from the point of view of characteristic variables. Ocean Modelling 9, 231–252.

Borges, R., Carmona, M., Costa, B., Don, W.S., 2008. An improved weighted essentially non-oscillatory scheme for hyperbolic conservation laws. Journal of Computational Physics 227, 3191 – 3211.

Burchard, H., Petersen, O., Rippeth, T.P., 1998. Comparing the performance of the mellor-yamada and the $k-\epsilon$ two-equation turbulence models. Journal of Geophysical Research: Oceans 103, 10543–10554.

Cheng, Z., Hsu, T.J., Calantoni, J., 2017. Sedfoam: A multi-dimensional eulerian two-phase model for sediment transport and its application to momentary bed failure. Coastal Engineering 119, 32–50.

606 Cox, D.T., Kobayashi, N., Okayasu, A., 1994. Vertical Variations of Fluid Velocities and Shear Stress in
607 Surf Zones. pp. 98–112.
608 Debreu, L., Marchesiello, P., Penven, P., Cambon, G., 2012. Two-way nesting in split-explicit ocean models:
609 Algorithms, implementation and validation. Ocean Modelling 49–50, 1 – 21.
610 Derakhti, M., Kirby, J.T., 2014. Bubble entrainment and liquid–bubble interaction under unsteady breaking
611 waves. Journal of Fluid Mechanics 761, 464–506.
612 Derakhti, M., Kirby, J.T., Shi, F., Ma, G., 2016. Nhwave: Consistent boundary conditions and turbulence
613 modeling. Ocean Modelling 106, 121 – 130.
614 Devolder, B., Troch, P., Rauwoens, P., 2018. Performance of a buoyancy-modified $k-\omega$ and $k-\omega$ sst
615 turbulence model for simulating wave breaking under regular waves using openfoam. Coastal Engineering
616 138, 49–65.
617 Dibajnia, M., Watanabe, A., 1992. Sheet flow under nonlinear waves and currents. Coastal Engineering
618 Proceedings 1.
619 Dohmen-Janssen, C., Kroekenstoel, D.F., Hassan, W.N., Ribberink, J.S., 2002. Phase lags in oscillatory
620 sheet flow: experiments and bed load modelling. Coastal Engineering 46, 61–87.
621 Drake, T.G., Calantoni, J., 2001. Discrete particle model for sheet flow sediment transport in the nearshore.
622 Journal of Geophysical Research: Oceans 106, 19859–19868.
623 Durran, D.R., 2010. Numerical Methods for Fluid Dynamics: With Applications to Geophysics. volume 32
624 of Texts in Applied Mathematics. Springer.
625 Elgar, S., Gallagher, E.L., Guza, R.T., 2001. Nearshore sandbar migration. Journal of Geophysical Research:
626 Oceans 106, 11623–11627.
627 Faria, A., Thornton, E., Lippmann, T., Stanton, T., 2000. Undertow over a barred beach. Journal of
628 Geophysical Research 105, 16999–17010.
629 Feddersen, F., Trowbridge, J., 2005. The effect of wave breaking on surf-zone turbulence and alongshore
630 currents: A modeling study. Journal of Physical Oceanography 35.
631 Grasso, F., Michallet, H., Barthélemy, E., 2011. Sediment transport associated with morphological beach
632 changes forced by irregular asymmetric, skewed waves. Journal of Geophysical Research: Oceans 116.
633 Hsu, T.J., Hanes, D.M., 2004. Effects of wave shape on sheet flow sediment transport. Journal of Geophysical
634 Research: Oceans 109.
635 Isobe, M., Horikawa, K., 1982. Study on water particle velocities of shoaling and breaking waves. Coastal
636 Engineering in Japan 25, 109–123.
637 Kalra, T., Sherwood, C., Warner, J., Rafati, Y., Hsu, T.J., 2019. Investigating bedload transport under
638 asymmetrical waves using a coupled ocean-wave model. pp. 591–604.
639 Kawanisi, K., Shiozaki, R., 2008. Turbulent effects on the settling velocity of suspended sediment. Journal

of Hydraulic Engineering 134, 261–266.

Kim, Y., Mieras, R.S., Cheng, Z., Anderson, D., Hsu, T.J., Puleo, J.A., Cox, D., 2019. A numerical study of sheet flow driven by velocity and acceleration skewed near-breaking waves on a sandbar using sedwavefoam. Coastal Engineering 152, 103526.

Larsen, B.E., van der A, D.A., van der Zanden, J., Ruessink, G., Fuhrman, D.R., 2020. Stabilized rans simulation of surf zone kinematics and boundary layer processes beneath large-scale plunging waves over a breaker bar. Ocean Modelling 155, 101705.

Li, M.Z., Amos, C.L., 2001. Sedtrans96: the upgraded and better calibrated sediment-transport model for continental shelves. Computers and Geosciences 27, 619–645. Numerical Models of Marine Sediment Transport and Deposition.

Lim, G., Jayaratne, R., Shibayama, T., 2020. Suspended sand concentration models under breaking waves: Evaluation of new and existing formulations. Marine Geology 426, 106197.

Lin, P., Liu, P.L.F., 1998. A numerical study of breaking waves in the surf zone. Journal of Fluid Mechanics 359, 239–264.

Malarkey, J., Davies, A., 2012. Free-stream velocity descriptions under waves with skewness and asymmetry. Coastal Engineering 68, 78–95.

Marchesiello, P., Auclair, F., Debreu, L., McWilliams, J., Almar, R., Benshila, R., Dumas, F., 2021. Tridimensional nonhydrostatic transient rip currents in a wave-resolving model. Ocean Modelling 163, 101816.

Marchesiello, P., McWilliams, J.C., Shchepetkin, A., 2001. Open boundary conditions for long-term integration of regional oceanic models. Ocean modelling 3, 1–20.

Mayer, S., Madsen, P.A., 2000. Simulation of Breaking Waves in the Surf Zone using a Navier-Stokes Solver. pp. 928–941.

McWilliams, J.C., Restrepo, J.M., Lane, E.M., 2004. An asymptotic theory for the interaction of waves and currents in coastal waters. Journal of Fluid Mechanics 511, 135–178.

Michallet, H., Ruessink, B.G., Vieira Lima Matias da Rocha, M., De Bakker, A., Van Der A, D.A., Ruju, A., Silva, P.A., Sénéchal, N., Marieu, V., Tissier, M., Almar, R., Abreu, T., Birrien, F., Vignal, L., Barthélemy, E., Mouazé, D., Cienfuegos, R., Wellens, P., 2014. GLOBEX: Wave dynamics on a shallow sloping beach, in: HYDRALAB IV Joint User Meeting, Lisbon, July 2014, Lisbonne, Portugal. pp. 1–12.

Nam, P.T., Staneva, J., Thao, N.T., Larson, M., 2020. Improved calculation of nonlinear near-bed wave orbital velocity in shallow water: Validation against laboratory and field data. Journal of Marine Science and Engineering 8.

Otsuka, J., Saruwatari, A., Watanabe, Y., 2017. Vortex-induced suspension of sediment in the surf zone. Advances in Water Resources 110, 59–76.

Rafati, Y., Hsu, T.J., Elgar, S., Raubenheimer, B., Quataert, E., van Dongeren, A., 2021. Modeling the

hydrodynamics and morphodynamics of sandbar migration events. Coastal Engineering 166, 103885.

Reniers, A.J.H.M., Roelvink, J.A., Thornton, E.B., 2004. Morphodynamic modeling of an embayed beach under wave group forcing. Journal of Geophysical Research: Oceans 109.

Ribas, F., de Swart, H., Calvete, D., Falqués, A., 2011. Modeling waves, currents and sandbars on natural beaches: The effect of surface rollers. Journal of Marine Systems 88, 90–101. 41st International Liege Colloquium on Ocean Dynamics"Science based management of the coastal waters.

Roelvink, D., Roelvink, J., Reniers, A., 2012. A Guide to Modeling Coastal Morphology. Advances in coastal and ocean engineering, World Scientific.

Roelvink, J., 2006. Coastal morphodynamic evolution techniques. Coastal Engineering 53, 277–287. Coastal Hydrodynamics and Morphodynamics.

Roelvink, J.A., Reniers, 1995. IP 11D delta flume experiments : a dataset for profile model validation. WL / Delft Hydraulics.

Roelvink, J.A., Stive, M.J.F., 1989. Bar-generating cross-shore flow mechanisms on a beach. Journal of Geophysical Research: Oceans 94, 4785–4800.

Ruessink, B.G., Michallet, H., Abreu, T., Sancho, F., Van der A, D.A., Van der Werf, J.J., Silva, P.A., 2011. Observations of velocities, sand concentrations, and fluxes under velocity-asymmetric oscillatory flows. Journal of Geophysical Research: Oceans 116.

Schnitzler, B., 2015. Modeling sand transport under breaking waves.

Scott, N.V., Hsu, T.J., Cox, D., 2009. Steep wave, turbulence, and sediment concentration statistics beneath a breaking wave field and their implications for sediment transport. Continental Shelf Research 29, 2303–2317.

Shchepetkin, A.F., McWilliams, J.C., 2005. The regional oceanic modeling system (roms): a split-explicit, free-surface, topography-following-coordinate oceanic model. Ocean Modelling 9, 347–404.

Smith, J.D., McLean, S.R., 1977. Spatially averaged flow over a wavy surface. Journal of Geophysical Research (1896-1977) 82, 1735–1746.

Soufflet, Y., Marchesiello, P., Lemarié, F., Jouanno, J., Capet, X., Debreu, L., Benshila, R., 2016. On effective resolution in ocean models. Ocean Modelling 98, 36–50.

Soulsby, R., 1995. Bed shear stresses due to combined waves and currents, in: Stive, M., Fredsøe, J., Hamm, L., Soulsby, R., Teisson, C., Winterwerp, J. (Eds.), Advances in Coastal Morphodynamics, Delft Hydraulics, Delft, The Netherlands. pp. 420–423.

Soulsby, R., 1997. Dynamics of marine sands. Thomas Telford Publishing.

Soulsby, R., Whitehouse, R., 1997. Threshold of sediment motion in coastal environments.

Stive, M., 1986. A model for cross-shore sediment transport, in: Procedings of the 20th International Conference on Coastal Engineering, American Society of Civil Engineers, New York.

Suarez, L., Barthelemy, E., Berni, C., Chauchat, J., Michallet, H., Cienfuegos, R., 2014. Vertical distribution of skewness and asymmetry in a boundary layer on a mobile bed. experiment and k-ω comparison. La Houille Blanche , 88–94.

Svendsen, I., 1987. Analysis of surf zone turbulence. Journal of Geophysical Research: Oceans 92, 5115–5124.

Thornton, E.B., Humiston, R.T., Birkemeier, W., 1996. Bar/trough generation on a natural beach. Journal of Geophysical Research: Oceans 101, 12097–12110.

Ting, F.C., Kirby, J.T., 1994. Observation of undertow and turbulence in a laboratory surf zone. Coastal Engineering 24, 51–80.

van der A, D.A., Ribberink, J.S., van der Werf, J.J., O'Donoghue, T., Buijsrogge, R.H., Kranenburg, W.M., 2013. Practical sand transport formula for non-breaking waves and currents. Coastal Engineering 76, 26–42.

van der Zanden, J., van der A, D., Hurther, D., Cáceres, I., O'Donoghue, T., Ribberink, J., 2017. Suspended sediment transport around a large-scale laboratory breaker bar. Coastal Engineering 125, 51–69.

van Rijn, L., Walstra, D., Grasmeijer, B., Sutherland, J., Pan, S., Sierra, J., 2003. The predictability of cross-shore bed evolution of sandy beaches at the time scale of storms and seasons using process-based profile models. Coastal Engineering 47, 295–327.

Veen, R., 2014. The implementation and testing of the santoss sand transport model in delft3d.

Voulgaris, G., Collins, M., 2000. Sediment resuspension on beaches: response to breaking waves. Marine Geology 167, 167–187.

Warner, J., Sherwood, C., Arango, H., Signell, R., 2005. Performance of four turbulence closure methods implemented using a generic length scale method. Ocean Modelling 8, 81–113.

Warner, J.C., Defne, Z., Haas, K., Arango, H.G., 2013. A wetting and drying scheme for ROMS. Computers and Geosciences 58, 54 – 61.

Warner, J.C., Sherwood, C.R., Signell, R.P., Harris, C.K., Arango, H.G., 2008. Development of a three-dimensional, regional, coupled wave, current, and sediment-transport model. Computers & Geosciences 34, 1284–1306.

Watanabe, A., 1982. Numerical models of nearshore currents and beach deformation. Coastal Engineering in Japan 25, 147–161.

Watanabe, Y., Saeki, H., 1999. Three-dimensional large eddy simulation of breaking waves. Coastal Engineering Journal 41, 281–301.

van der Werf, J., Veen, R., Ribberink, J., van der Zanden, J., 2015. Testing of the new santoss transport formula in the Delft3d morphological modeling system.

Wiberg, P.L., Rubin, D.M., 1989. Bed roughness produced by saltating sediment. Journal of Geophysical Research: Oceans 94, 5011–5016.

742 Wilcox, D.C., 1988. Reassessment of the scale-determining equation for advanced turbulence models. AIAA
743 Journal 26, 1299–1310.
744 Zijlema, M., Stelling, G., Smit, P., 2011. Swash: An operational public domain code for simulating wave
745 fields and rapidly varied flows in coastal waters. Coastal Engineering 58, 992 – 1012.

Table 1: LIP experiment conditions from Roelvink and Reniers (1995)

Experiment	Initial Geometry	H_S [m]	T_P [s]	Duration [h]	Collection [h]
LIP11-1A	Initial beach profile	0.9	5	12	
LIP11-1B	Result of 1A	1.4	5	18	8
LIP11-1C	Result of 1B	0.6	8	13	7

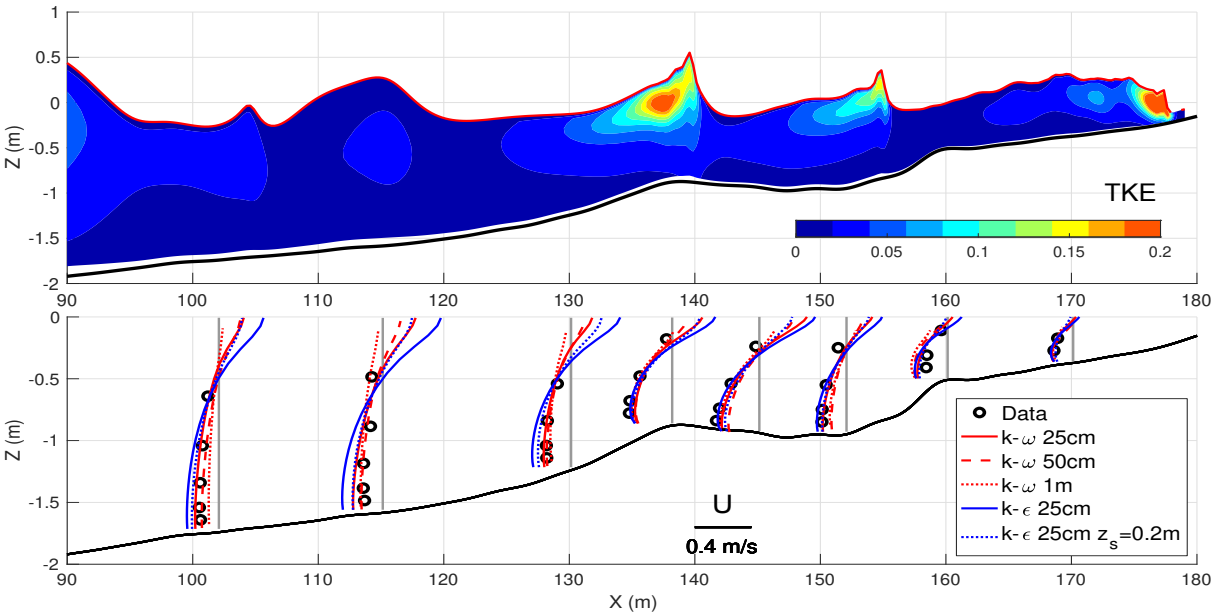

Figure 1: Model comparison with the large-scale LIP11-1B Flume experiment. Top) Snapshot of wave height and turbulent kinetic energy k $[m^2/s^2]$ from the reference model simulation (25 cm resolution; k-ω turbulence model). Bottom) Comparison of simulated and measured cross-shore current profiles: sensitivity to resolution (25 cm, 50 cm and 1 m) and turbulence models (k-ω in red; k-ϵ in blue).

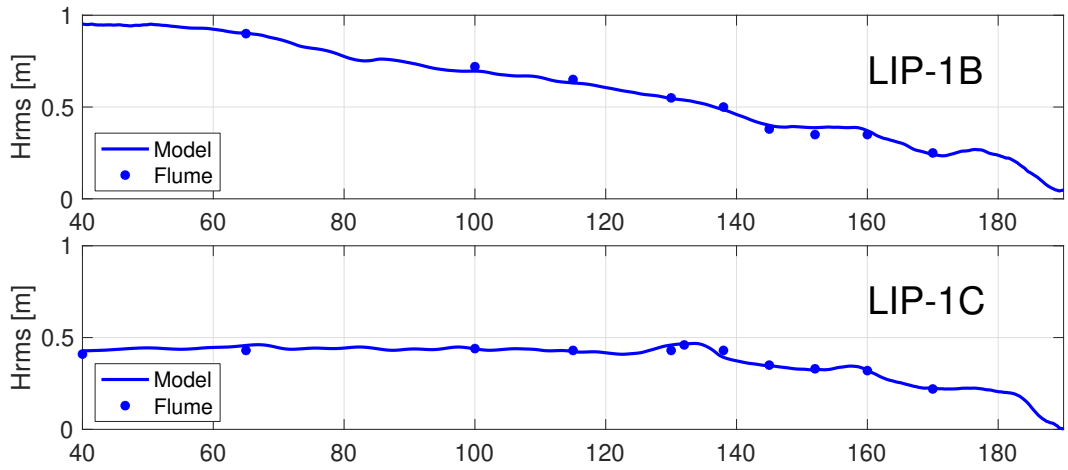

Figure 2: Model-data comparison of H_{rms} in LIP Flume experiment (top: 1B; bottom: 1C).

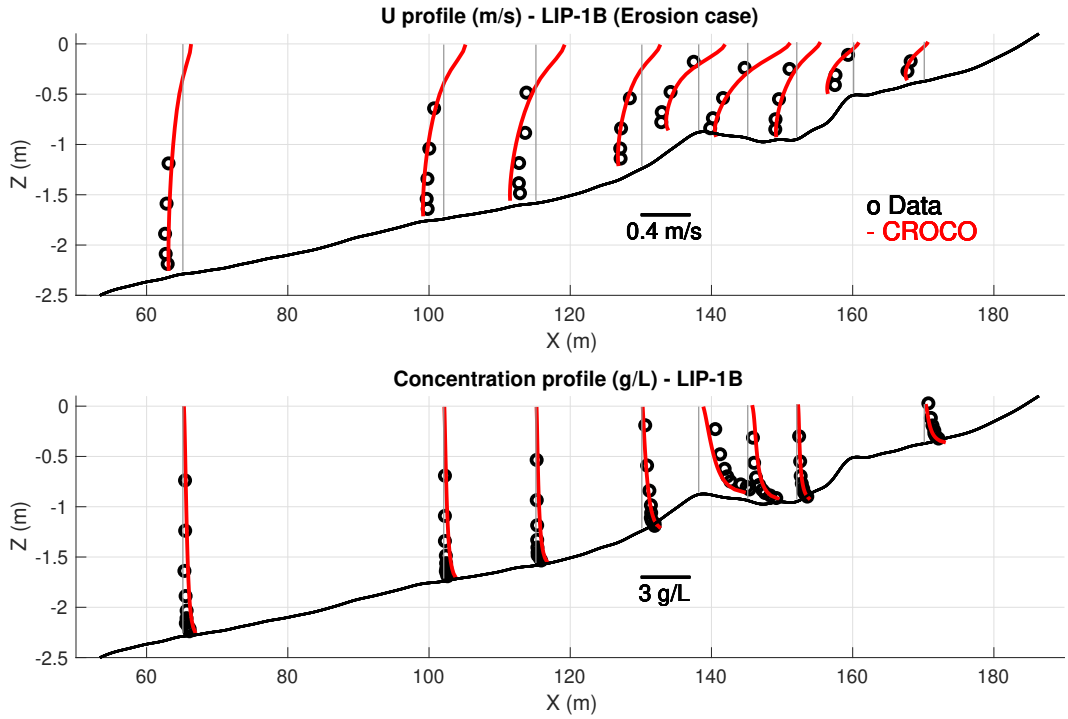

Figure 3: Model-data comparison of wave-mean cross-shore velocity and sand concentration profiles in the erosive LIP11-1B Flume experiment.

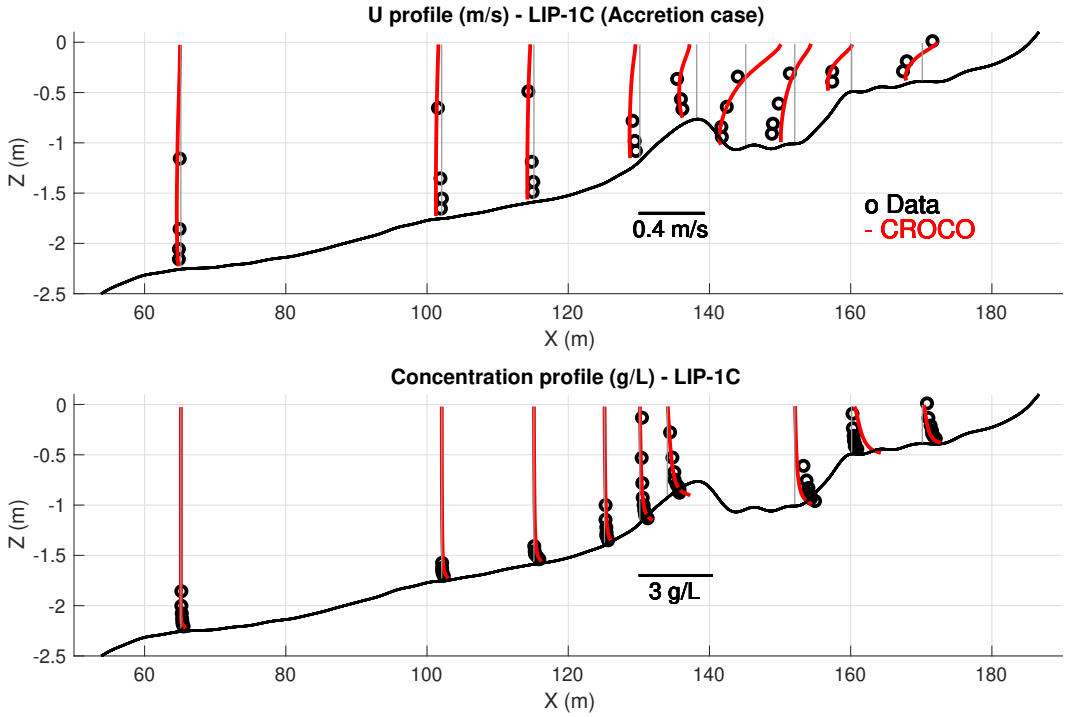

Figure 4: Model-data comparison of wave-mean cross-shore velocity and sand concentration profiles in the accretive LIP11-1C Flume experiment.

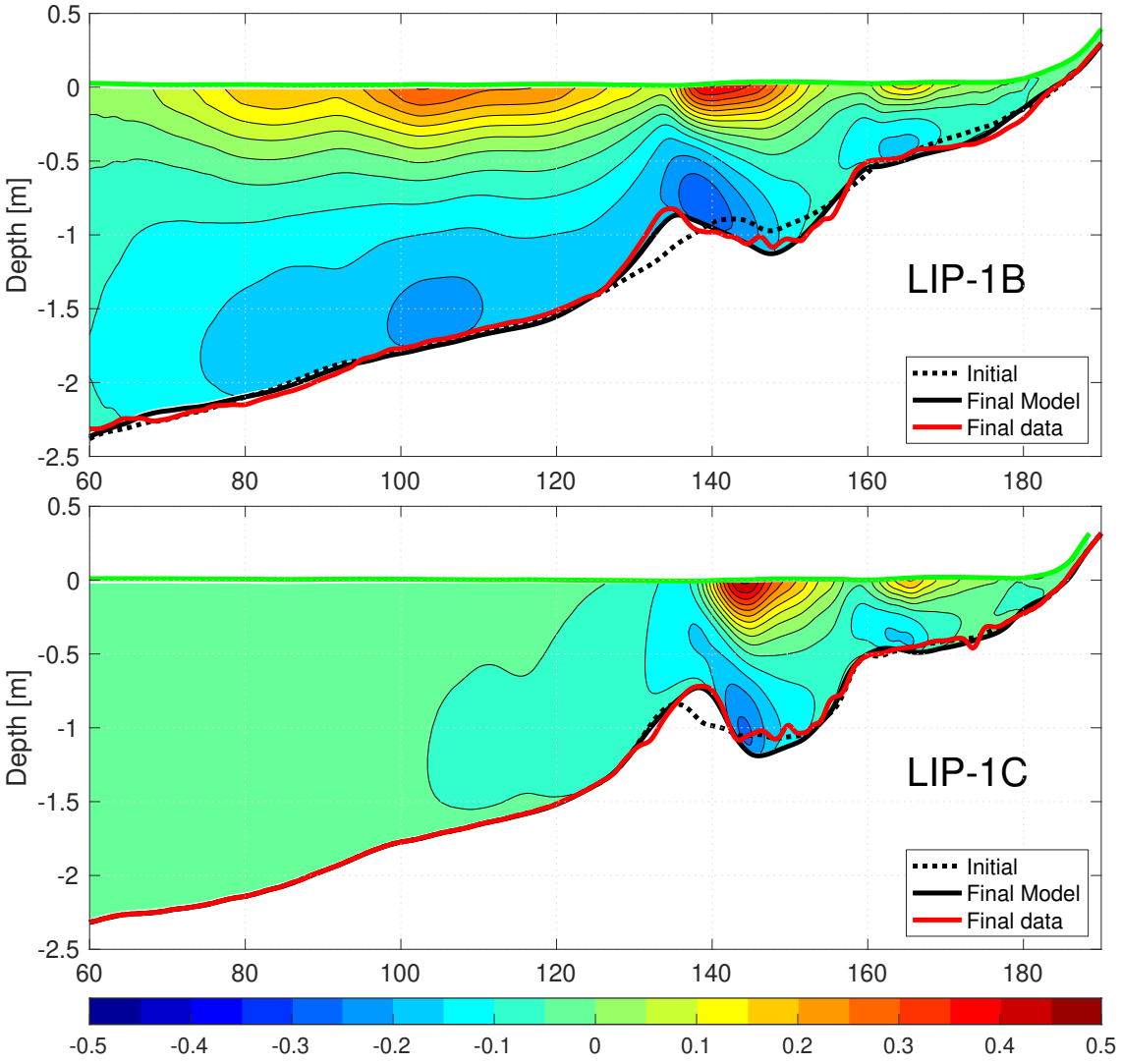

Figure 5: Model comparison of morphological changes with LIP measurements during the erosion phase (LIP-1B) and accretion phase (LIP-1C). Wave-mean cross-shore velocities are also shown in filled contours [m/s].

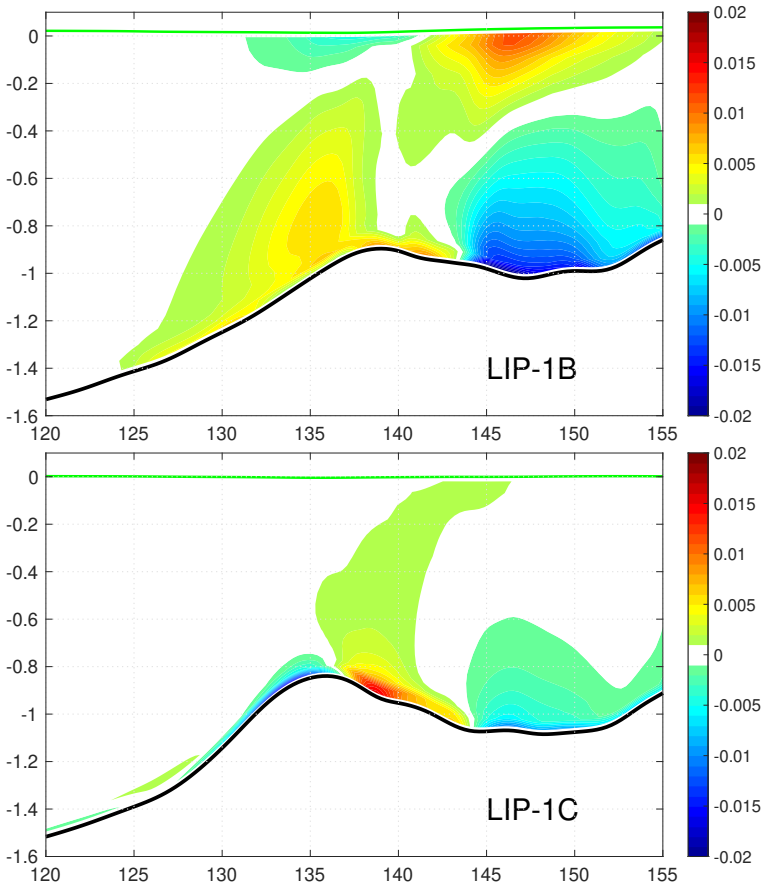

Figure 6: Wave-mean sand advection [kg/m^3/s] halfway through the erosion phase (LIP-1B) and accretion phase (LIP-1C).

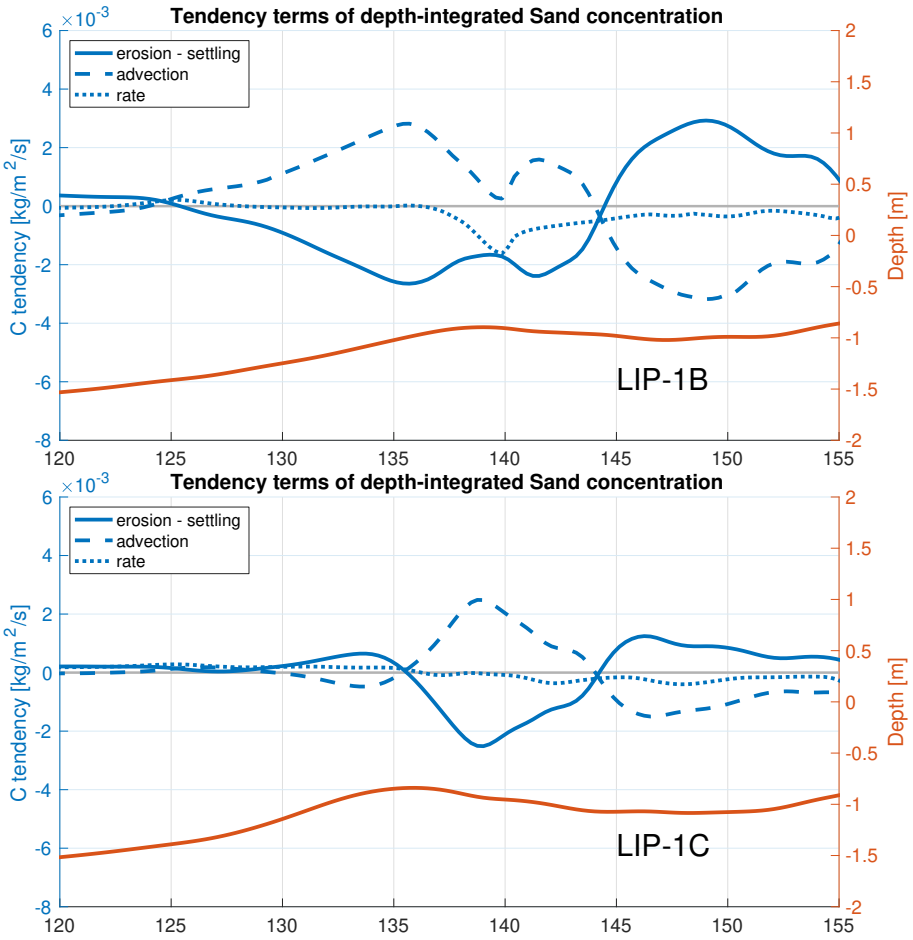

Figure 7: Depth-integrated budget of sand concentration halfway through the erosion phase (LIP-1B) and accretion phase (LIP-1C).

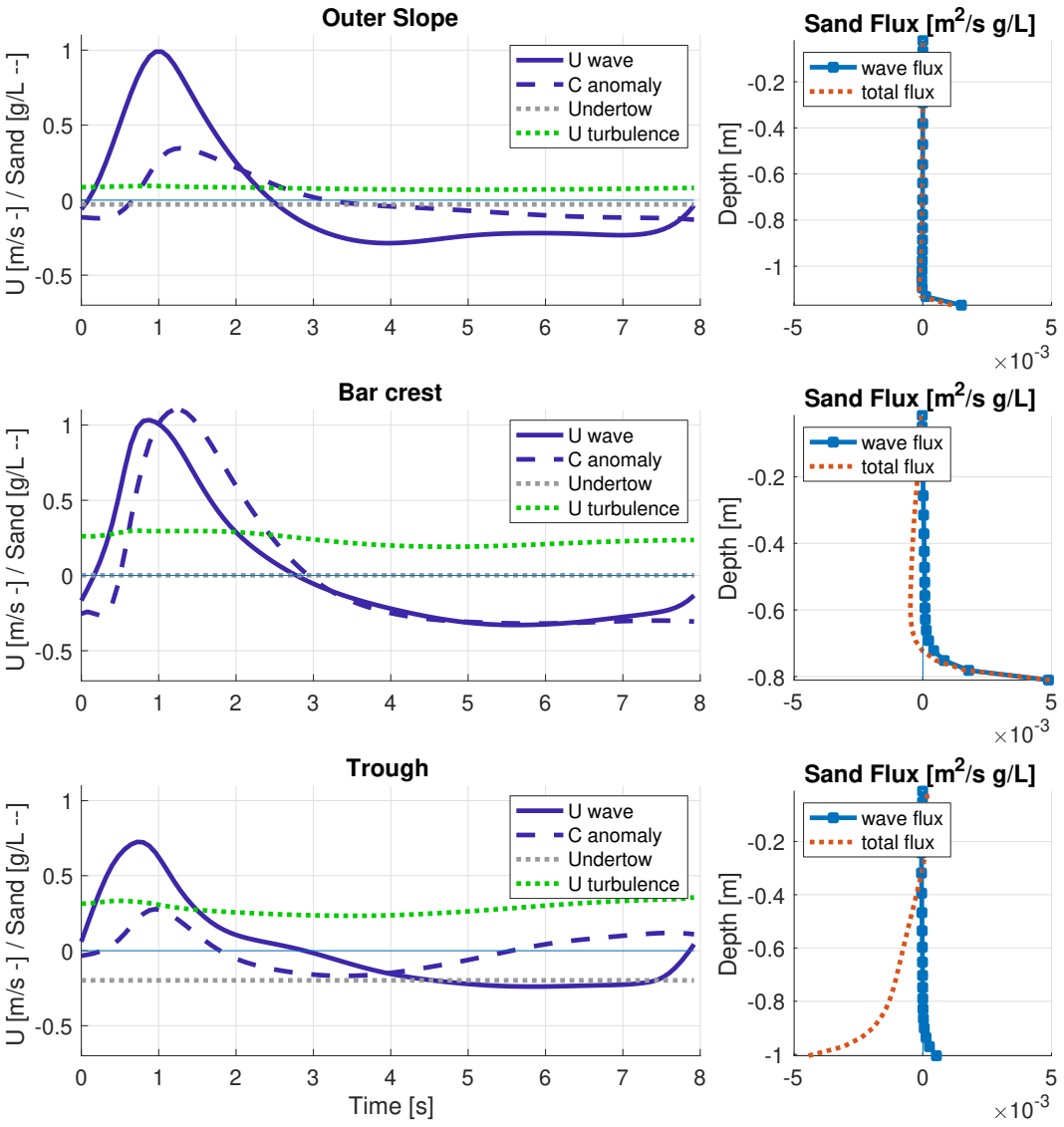

Figure 8: Left panels: composite wave cycle of current and sand concentration anomaly ($u' = u - \overline{u}$ and $C' = C - \overline{C}$) at three positions over the sandbar during the accretive LIP-1C Flume experiment. The wave-mean undertow u_b and mean effective turbulent velocity u_t at the bottom level z_b are also represented. Right panels: profiles of suspended sand flux (total flux: $\overline{uC}$; and wave flux: $\overline{u'C'}$).

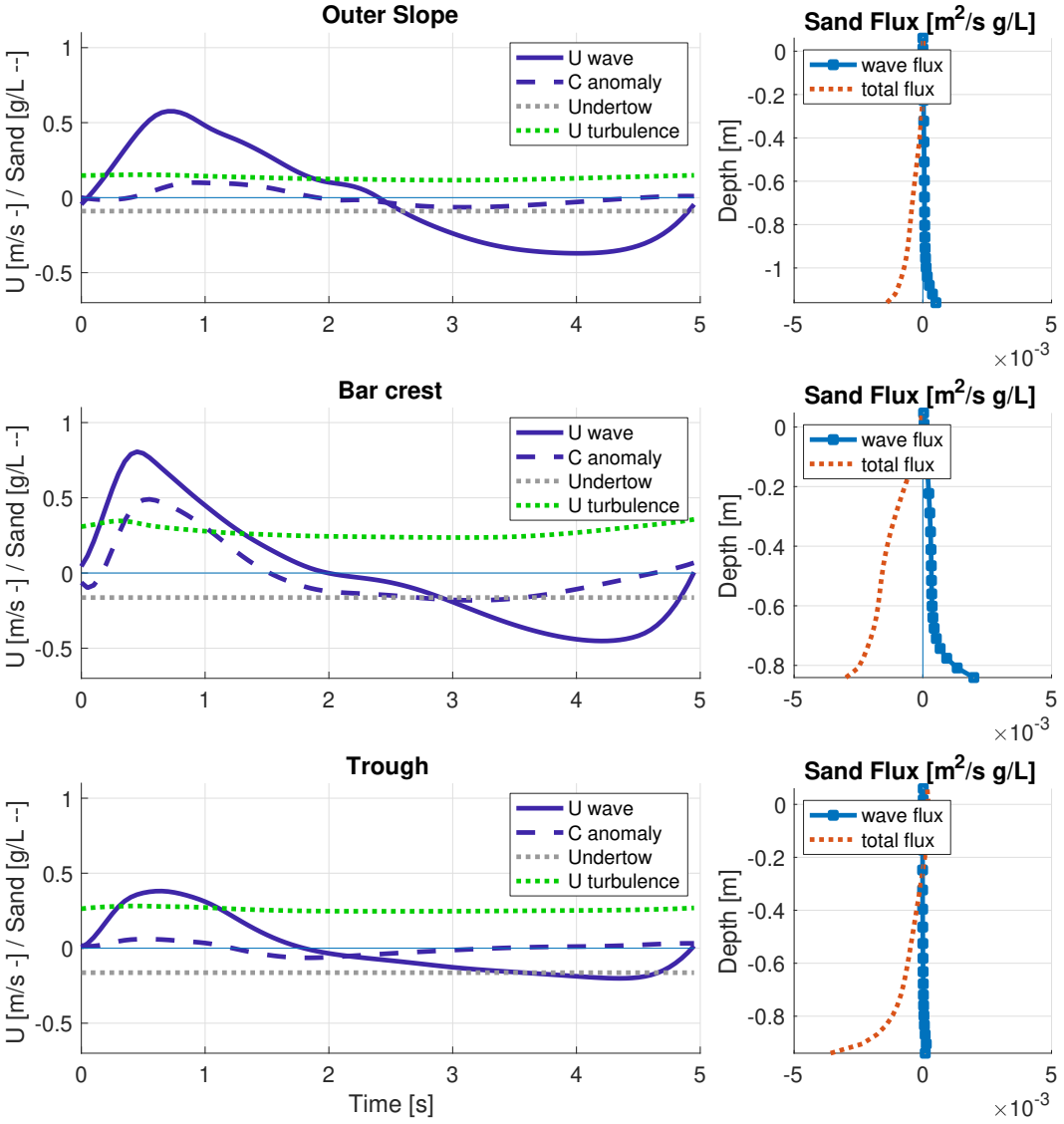

Figure 9: Same as Figure 8 but for the LIP-1B Flume experiment.

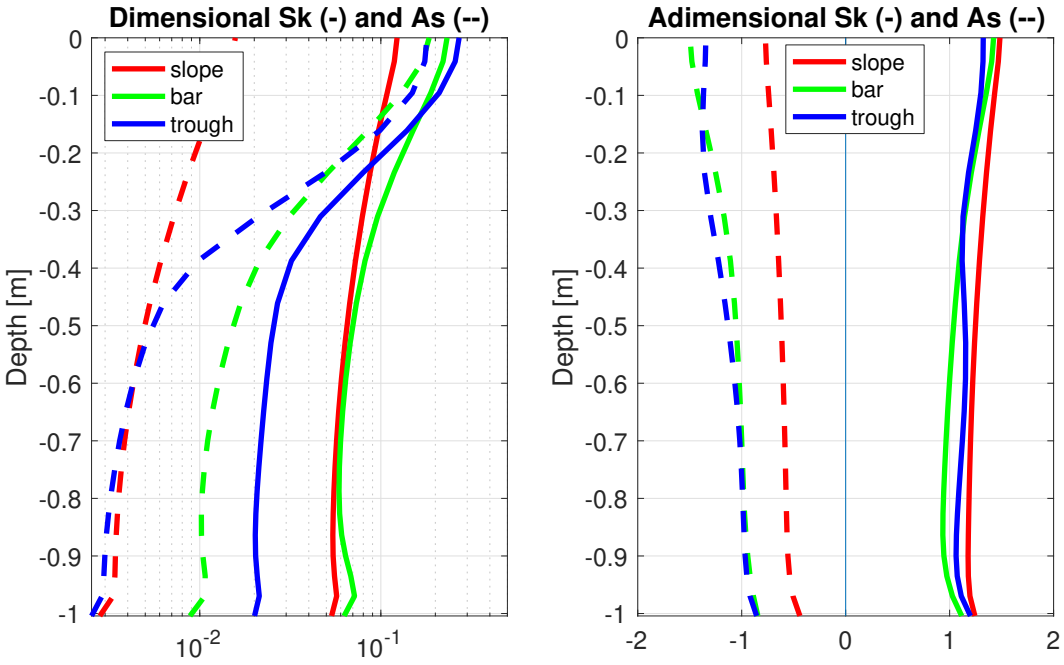

Figure 10: Composite analysis of wave asymmetry and skewness profiles (absolute and normalized) at three locations around the sandbar, during the accretive LIP-1C Flume experiment. Asymmetry is represented by dashed lines, skewness by solid lines.

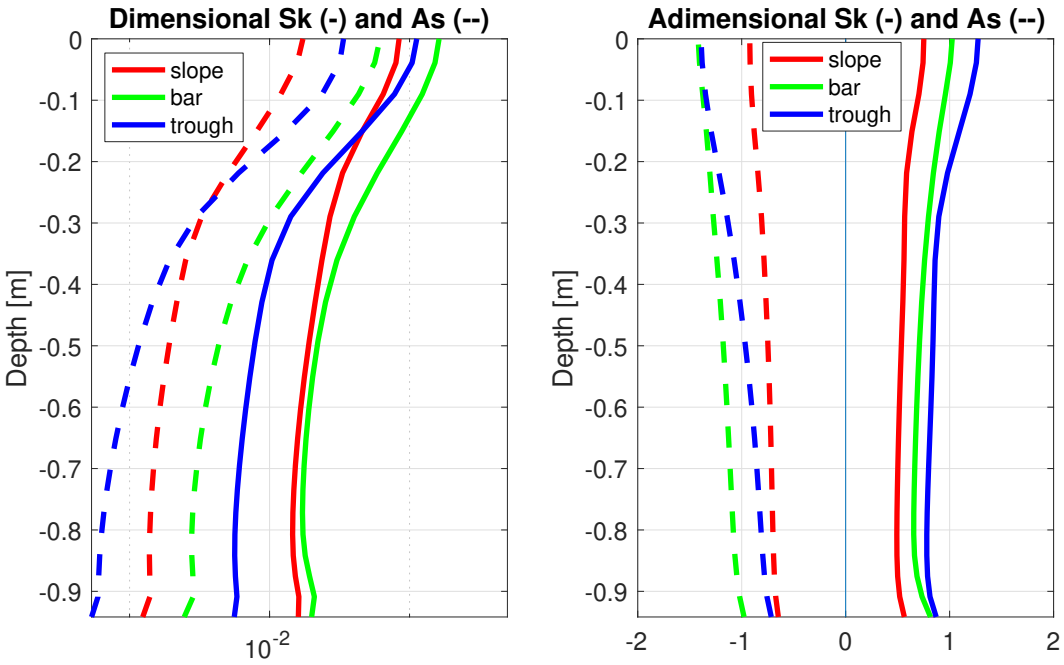

Figure 11: Composite analysis of wave asymmetry and skewness profiles (dimensional and dimensionless) at three locations around the sandbar, during the erosive LIP-1B Flume experiment.

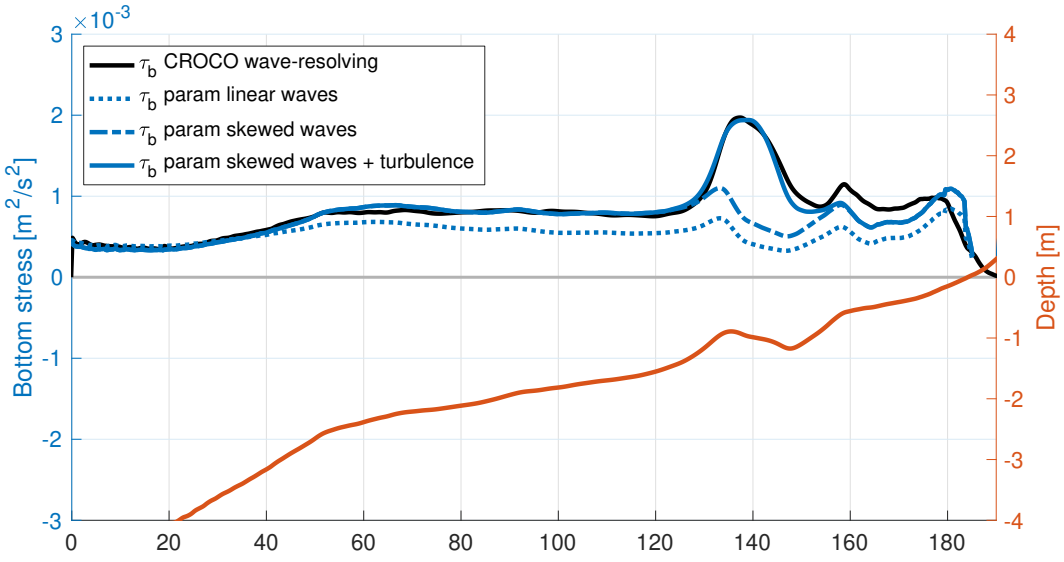

Figure 12: Bed shear stress profiles from the wave-resolving model and reconstructed from empirical formulations using wave-averaged values and linear wave theory with or without skewness correction.